Table 3. Late genitourinary and gastrointestinal toxicities

	Grade		
	0	1	2
Genitourinary	25	2	3
Frequency/urgency	28	0	2
Urinary retention	30	0	0
Painful urination	29	1	0
Hematuria	28	1	1
Gastrointestinal	19	8	3
Proctitis	27	3	0
Rectal bleeding	20	7	3
Proctalgia	30	0	0

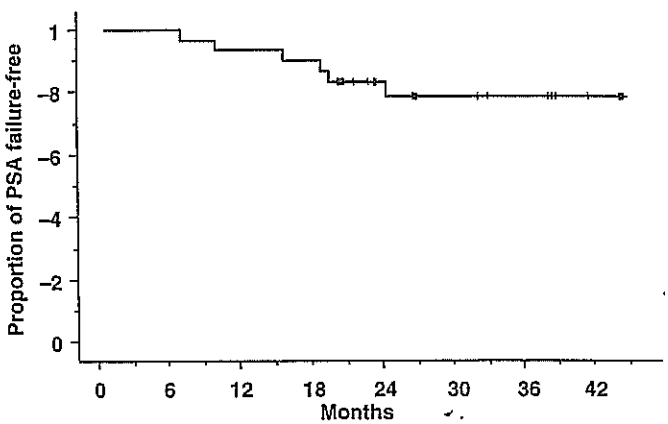

Figure 3. PSA-failure free survival for all patients.

control rate was obtained as the radiation dose to the prostate increased to >70 Gy. Regarding toxicity it was also reported that serious complications drastically increased when using doses >70 Gy, if the conventional radiation technique was used (3,4). As computed radiography and radiotherapy devices developed, more precise radiotherapy techniques were put into clinical use, such as 3D-CRT, IMRT, particle therapy and brachytherapy. These techniques can allow good target dose coverage with a minimal dose to the surrounding normal tissue when performing high-dose radiotherapy for prostate cancer.

Many institutions have tried to conduct high-dose external beam radiotherapy with >70 Gy for prostate cancer using 3D-CRT or IMRT (5–8). They reported satisfactory clinical outcomes of high-dose radiotherapy for prostate cancer, including both efficacies and morbidities, but these single institutional data cannot confirm the usefulness of high-dose radiotherapy as a standard treatment for prostate cancer. To evaluate the safety and to determine the recommendable dose of high-dose radiotherapy, RTOG started to conduct a dose escalation study (RTOG 9406) using 3D-CRT (9–11). The patient accrual has finished and the safety of high-dose 3D-CRT will be confirmed. There are several large series treating patients with localized prostate cancer by using permanent implant brachytherapy with or without external beam radiotherapy for >10 years (14–16). To confirm these retrospective data, RTOG also started to conduct prospective studies of permanent implant brachytherapy with or without external beam radiotherapy.

Until now, there have been two phase III studies with final results, comparing high-dose with standard-dose radiotherapy for prostate cancer. One was conducted by MGH using proton boost therapy (24), and the other was conducted by MD Anderson Cancer Center using 3D-CRT (25). In the MGH trial, patients with T3-T4NX/N0-2 prostate cancer received 67.2 Gy by photon radiotherapy or 75.6 Gy by photon/proton combined therapy. There was no significant difference between the two groups in any survival outcome. In the MD Anderson trial, 305 patients with T1–T3 prostate cancer were randomized to receive a standard-dose of 70 Gy or a high-dose of 78 Gy. The freedom from failure rate at 6 years in the high-dose group (74%) was significantly better than that in the standard-dose group (64%). To assess the efficacy of high-dose radiotherapy in a multi-institutional setting, RTOG is now conducting a phase III study comparing a high-dose of 82.28 Gy with a standard-dose of 72.93 Gy for prostate cancer.

Thus although there are many promising outcomes and wide experiences of high-dose radiotherapy for prostate cancer, the topic remains under investigation and the optimal dose for each risk group has not been established.

PBT for Prostate Cancer

PBT for prostate cancer started at MGH in the 1970s (18). In the phase III trial previously described, there was no significant difference in survival outcomes between high-dose and standard-dose groups (24). At LLUMC, >1200 patients with prostate cancer were treated by PBT. They used photon radiotherapy to the pelvis at 45 Gy followed by proton boost to the prostate at 30 Gy for high-risk patients, and PBT alone with a total dose of 74 Gy for low-risk patients. The overall 5 year and 8 year actuarial biochemical disease-free survival rates were 75 and 73%, respectively (26,27). MGH and LLUMC cooperatively completed the phase III trial using proton boost therapy following photon radiotherapy, which randomized patients with early prostate cancer to receive a dose of 70.2 or 79.2 Gy. They are now conducting another dose escalation phase I/II study using >80 Gy of PBT alone.

In Japan, PBT was first used at Tsukuba University in 1985. They experienced PBT with 14 prostate cancer patients, but the evaluation was performed retrospectively and this cannot be considered as an establishment of policy for PBT for prostate cancer in Japan. In NCCHE, PBT was applied to clinical use in 1998, and the present study for prostate cancer started in 2001. Owing to the small number of patients and short duration of follow-up, the effectiveness of PBT for prostate cancer should not be assessed from the current study. However, because no patient experienced any grade 3 or greater toxicities, the feasibility of the proton boost therapy following photon radiotherapy was confirmed.

Dose Distribution and Toxicities

We analysed the rectal DVHs using the current study cohort. The rectal DVHs in the photon/proton combined therapy (the current study) were compared with those produced by planning in PBT alone. Figure 4 shows the apparent advantage of the rectal DVHs using PBT alone compared with those using photon/proton combined treatment (28). In that study, the rectal DVH using PBT alone was much superior to the DVH constraints of 3D-CRT and just comparable to those of IMRT introduced by other institutions and clinical trials.

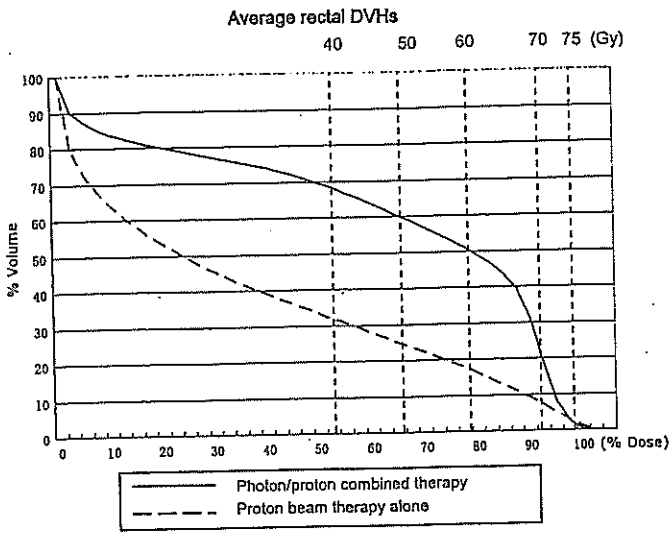

Figure 4. Comparison of average rectal DVHs between photon/proton combined therapy and proton therapy alone.

Comparison of late GI toxicities between other series of external radiation therapy is shown in Table 4. The frequency of late grades 2 and 3 GI toxicities in RTOG 9406 (11) was less than that of other reports, but this was probably owing to the lower total doses with a smaller fraction size of 1.8 Gy rather than 2.0 Gy. LLUMC reported 21% late grade 2 GI toxicities in patients who received photon/proton combined therapy or PBT alone (27). Because they considered isolated rectal bleeding (grade 1) and transfusion (grade 3) as grade 2, the true frequency of late grade 2 GI toxicities was supposed to be <21%. Table 4 shows that the frequency of grades 1 and 2 late rectal toxicities in the current study was comparable to that of other reports using high-dose external beam radiotherapy.

As the RTOG 9406 study reported, severe late toxicities (grade 3) significantly decreased using 3D-CRT compared with those observed in historical studies using conventional radiotherapy. However, moderate late toxicities (grade 1/2) were unexpectedly increased by high-dose radiotherapy using 3D-CRT (11). Grades 1 and 2 toxicities are not severe but have a significant impact on a patients' quality of life, so it becomes a matter of great importance how we can reduce both severe and moderate late toxicities. As shown in Table 4, Memorial Sloan Kettering Cancer Center reported reduced actuarial incidences of moderate toxicities (grade 2) by using IMRT, even with a higher dose level (6). As described above, because PBT alone can produce rectal DVH just as well as IMRT, it is expected that not only grade 3 but grade 1/2 toxicities can be reduced by using PBT alone, at least to the same extent as when using IMRT. And the discussion thus far about rectal toxicities can also be applied to GU and other toxicities.

Table 4. Comparison of late gastrointestinal toxicities between other reports

Institution/study (reference no.)	Dose (Gy)	Radiation technique	Grade			Years
			1	2	3	
MSKCC phase I/II (5,6)	64.8–81	3D-CRT	16%	10%	1%	5
	75.6–81	3D-CRT	–	14%	–	5
	81	3D-CRT	–	12%	2%	3
	81	IMRT	–	2%	0.5%	3
MDACC phase III (8)	78	3D-CRT	28%	19%	7%	6
				23% (grade 2/3)		2
	70	3D-CRT	36%	11%	1%	6
				12% (grade 2/3)		2
RTOG 94-06 (9,10)	68.4	3D-CRT	–	9% (grade 2/3)		3.1
	73.8	3D-CRT	–	9% (grade 2/3)		2.2
	79.2	3D-CRT	24%	8% (grade 2/3)		3.1–3.6
LLUMC (27)	74–75	Photon/proton and proton alone	–	21%	–	3
The current study	76	Photon/proton	27%	10%	0%	2.5

MSKCC, Memorial Sloan Kettering Cancer Center; MDACC, MD Anderson Cancer Center; RTOG, Radiation Therapy Oncology Group; LLUMC, Loma Linda University Medical Center.

COMPARISON WITH IMRT

By using IMRT, multiple portals of photon beams three-dimensionally expose a large volume of the surrounding normal tissues to low radiation doses. In contrast, PBT alone can generate sufficient dose coverage to the prostate by lateral opposed portals with no radiation exposure to the ventral and dorsal portion of the body (Fig. 1b). Discussed from such a viewpoint as difference in physical characteristics between photon and proton beams, it is suggested that PBT alone can further reduce the toxicity compared with IMRT. Because of using just lateral opposed portals, the conformity of the prescribed dose to the target volume by PBT is poorer than that by IMRT, but intensity-modulated proton therapy which is now developing for clinical application will improve the conformity of the current PBT and realize more ideal dose painting in the target volume in the future (29).

Regarding the risk of second malignancy as long-term sequelae, Brenner et al. (30) reported interesting data from the Surveillance, Epidemiology and End Results (SEER) Program cancer registry (1973–93). Radiotherapy for prostate cancer was associated with a small but statistically significant increase in the risk of second solid tumors, particularly for long-term survivors, relative to treatment with surgery. By sparing the large volume of the surrounding normal tissues from exposure of low radiation doses, it is expected that using PBT to treat prostate cancer can decrease the risk of radiation-related second malignancy. Diagnosis at younger ages and earlier stages is resulting in longer survival times for patients with prostate cancer, and radiation-related second malignancy risk becomes a more significant issue in the future.

FUTURE DIRECTIONS

Although MGH and LLUMC have large experiences using PBT, the data of retrospective analysis and combination with photon therapy were included. A multi-institutional prospective clinical trial can further confirm the efficacy and safety of proton therapy. As discussed above, because the dose distribution generated by PBT alone is superior to that by photon/proton combined treatment (the current study), the feasibility of the current study should warrant the safety of PBT alone for prostate cancer with the same total dose. There are now five institutions with proton facilities in Japan, and we are conducting a multi-institutional phase II trial in which we treat low- and intermediate-risk prostate cancer by PBT alone with a total dose of 74 Gy_E. The primary endpoint is the incidence of grade 2 rectal bleeding at 2 years. This study will certainly confirm the clinical advantage of PBT for prostate cancer.

Acknowledgments

This paper was presented at the 40th semi-annual meeting of Particle Therapy Cooperative Group (PTCOG) in Paris, 2004.

References

1. Perez CA, Walz BJ, Zivnuska FR, Pilepich M, Prasad K, Bauer W. Irradiation of carcinoma of the prostate localized to the pelvis: analysis of tumor response and prognosis. *Int J Radiat Oncol Biol Phys* 1980;6:555–63.
2. Hanks GE, Martz KL, Diamond JJ. The effect of dose on local control of prostate cancer. *Int J Radiat Oncol Biol Phys* 1988;15:1299–305.
3. Pilepich MV, Krall JM, Sause WT, Johnson RJ, Russ HH, Hanks GE, et al. Prognostic factors in carcinoma of the prostate—analysis of RTOG study 75-06. *Int J Radiat Oncol Biol Phys* 1987;13:339–49.
4. Hanks GE. External-beam radiation therapy for clinically localized prostate cancer: patterns of care studies in the United States. *NCI Monogr* 1988;7:75–84.
5. Zelefsky MJ, Fuks Z, Hunt M, Lee HJ, Lombardi D, Ling CC, et al. High dose radiation delivered by intensity modulated conformal radiotherapy improves the outcome of localized prostate cancer. *J Urol* 2001;166:876–81.
6. Zelefsky MJ, Fuks Z, Hunt M, Yamada Y, Marion C, Ling CC, et al. High-dose intensity modulated radiation therapy for prostate cancer: early toxicity and biochemical outcome in 772 patients. *Int J Radiat Oncol Biol Phys* 2002;53:1111–6.
7. Hanks GE, Hanlon AL, Schultheiss TE, Pinover WH, Movasas B, Epstein BE, et al. Dose escalation with 3D conformal treatment: five year outcomes, treatment optimization, and future directions. *Int J Radiat Oncol Biol Phys* 1998;41:501–10.
8. Pollack A, Zagars GK. External beam radiotherapy dose response of prostate cancer. *Int J Radiat Oncol Biol Phys* 1997;39:1011–8.
9. Michalski JM, Purdy JA, Winter K, Roach M III, Vijayakumar S, Sandler HM, et al. Preliminary report of toxicity following 3D radiation therapy for prostate cancer on 3DOG/RTOG 9406. *Int J Radiat Oncol Biol Phys* 2000;46:391–402.
10. Ryu JK, Winter K, Michalski JM, Purdy JA, Markoe AM, Earle JD, et al. Interim report of toxicity from 3D conformal radiation therapy (3D-CRT) for prostate cancer on 3DOG/RTOG 9406, level III (79.2 Gy). *Int J Radiat Oncol Biol Phys* 2002;54:1036–46.
11. Michalski JM, Winter K, Purdy JA, Wilder RB, Perez CA, Roach M III, et al. Preliminary evaluation of low-grade toxicity with conformal radiation therapy for prostate cancer on RTOG 9406 dose level I and II. *Int J Radiat Oncol Biol Phys* 2003;56:192–8.
12. Blasko JC, Grimm PD, Ragde H. Brachytherapy and organ preservation in the management of carcinoma of the prostate. *Semin Radiat Oncol* 1993;3:240–9.
13. Blasko JC, Walker K, Grimm PD, Ragde H. Prostate specific antigen based disease control following ultrasound guided 125 Iodine implantation for stage T1/T2 prostatic carcinoma. *J Urol* 1995;154:1096–9.
14. Grimm PD, Blasko JC, Sylvester JE, Meier RM, Cavanagh W. 10-year biochemical (prostate-specific antigen) control of prostate cancer with 125 I brachytherapy. *Int J Radiat Oncol Biol Phys* 2001;51:31–40.
15. Sylvester JE, Blasko JC, Grimm PD, Meier R, Malmgren JA. Ten-year biochemical relapse-free survival after external beam radiation and brachytherapy for localized prostate cancer: the Seattle experience. *Int J Radiat Oncol Biol Phys* 2003;57:944–52.
16. Potters L, Morgenstern C, Mullen EE, Fearn P, Jassal A, Kattan M. Twelve year outcomes following permanent brachytherapy in patients with clinically localized prostate cancer. *Int J Radiat Oncol Biol Phys* 2004;60(Suppl):S183–4.
17. Archambeau JO, Bennett GW, Levine GS, Cowen R, Akanuma A. Proton radiation therapy. *Radiology* 1974;110:445–57.
18. Shipley WU, Tepper JE, Prout GR, Verhey LJ, Mendiondo OA, Goitein M, et al. Proton radiation as boost therapy for localized prostatic carcinoma. *J Am Med Assoc* 1979;241:1912–5.
19. Yonemoto LT, Slater JD, Rossi CJ, Antoine JE, Loredo L, Archambeau JO, et al. Combined proton and photon conformal radiation therapy for locally advanced carcinoma of the prostate: preliminary results of a phase I/II study. *Int J Radiat Oncol Biol Phys* 1997;37:21–9.
20. American Society for Therapeutic Radiology and Oncology Consensus Panel. Consensus statement: guidelines for PSA following radiation therapy. *Int J Radiat Oncol Biol Phys* 1997;37:1035–41.
21. Ando K, Furusawa Y, Suzuki M, Nojima H, Koike S, Aoki M, et al. Relative biological effectiveness of the 235 MeV proton beams at the National Cancer Center Hospital East. *J Radiat Res* 2001;42:79–89.
22. Ogino T, Murayama S, Itou Y, Nihei K, Kawashima M, Ishikura S, et al. Three-dimensional positioning verification by image subtraction method

using real-time digital radiography. *Int J Radiat Oncol Biol Phys* 2000;48(Suppl 1):195 (Abstr).
23. Nihei K, Ogino T, Ishikura S, Kawashima M, Murayama S, Ikeda H. Optimal PTV margin for proton therapy of prostate cancer: analysis of interfraction motion and patient position-related motion. *Radiother Oncol* 2002;64(Suppl 1):S274 (Abstr).
24. Shipley WU, Verhey LJ, Munzenrider JE, Suit HD, Urie MM, McManus PL, et al. Advanced prostate cancer: the results of a randomized comparative trial of high dose irradiation boosting with conformal protons compared with conventional dose irradiation using photons alone. *Int J Radiat Oncol Biol Phys* 1995;32:3–12.
25. Pollack A, Zagars GK, Starkschall G, Antolak JA, Lee JJ, Huang E, et al. Prostate cancer radiation dose response: results of the M. D. Anderson phase III randomized trial. *Int J Radiat Oncol Biol Phys* 2002;53:1097–105.
26. Slater JD, Rossi CJ, Yonemoto LT, Bush DA, Jabola BR, Levy RP, et al. Proton therapy for prostate cancer: the initial Loma Linda University experience. *Int J Radiat Oncol Biol Phys* 2004;59:348–52.
27. Slater JD, Yonemoto LT, Rossi CJ, Reyes-Molyneux NJ, Bush DA, Antonine JE, et al. Conformal proton therapy for prostate carcinoma. *Int J Radiat Oncol Biol Phys* 1998;42:299–304.
28. Nihei K, Nishio T, Ishikura S, Kawashima M, Ogino T. Analysis of dose volume histograms in proton therapy for prostate cancer. *Eur J Cancer* 2003;1(Suppl 5):S161.
29. Lomax A. Intensity modulation methods for proton radiotherapy. *Phys Med Biol* 1999;44:185–205.
30. Brenner DJ, Curtis RE, Hall EJ, Ron E. Second malignancies in prostate carcinoma patients after radiotherapy compared with surgery. *Cancer* 2000;88:398–406.

INSTITUTE OF PHYSICS PUBLISHING PHYSICS IN MEDICINE AND BIOLOGY

Phys. Med. Biol. 51 (2006) 1249–1260 doi:10.1088/0031-9155/51/5/014

Development of a simple control system for uniform proton dose distribution in a dual-ring double scattering method

Teiji Nishio[1], Shouji Kataoka[2], Masanori Tachibana[2], Kazutomo Matsumura[3], Naoya Uzawa[3], Hideki Saito[3], Toshinobu Sasano[4], Michiharu Yamaguchi[4] and Takashi Ogino[1]

[1] Particle Therapy Division, Research Center for Innovative Oncology, National Cancer Center, Kashiwa, Japan
[2] Sumitomo Heavy Industries Ltd, Japan
[3] SHI Accelerator Service Ltd, Japan
[4] Accelerate Engineering Company, Japan

Received 21 October 2005, in final form 26 December 2005
Published 15 February 2006
Online at stacks.iop.org/PMB/51/1249

Abstract

In proton radiotherapy with high focusing of irradiation on the tumour, it is important to obtain treatment beams with a highly uniform dose distribution. Uniform dose distribution in the clinical irradiation field can be obtained by the dual-ring double scattering method. This method is superior to the wobbler method, which uses electromagnetic deflection of the proton beams, because of the absence of the temporal structure of irradiation distribution. However, in the dual-ring double scattering method the condition of incident proton beams entering the scatter, especially the accuracy of the position of the incident proton beams with respect to the scatter, markedly affects the uniformity of the beam distribution in the irradiation field. In this study, to ensure the uniformity of dose distribution during treatment, we developed a control system equipped with an automatic fine adjustment of the beam axis and a mechanism for moving the second dual-ring scatter of the double scatters to the optimal position. Using this system, we achieved uniform dose distribution in the irradiation field during proton radiotherapy, with symmetry within ±1% and flatness within 2%.

(Some figures in this article are in colour only in the electronic version)

1. Introduction

Recently, radiotherapy using heavy-charged particle beams, such as proton beams and carbon beams, has been spreading throughout Japan and the world (PTCOG Newsletter 2004). Since heavy-charged particles have a charge, the beams are deflected in electromagnetic fields, and

multiple scattering and energy loss due to the Coulomb force occur when passing through substances. These properties are utilized for the formation of the irradiation field used for radiotherapy. In an irradiation field, uniformity of depth–dose distribution is formed by the bar-ridge filter or range modulator using energy loss resulting from the passing of particles through substances. The dual-ring double scattering method or wobbler method is used for a uniformly lateral dose distribution (Chu *et al* 1993, Graffman *et al* 1973, Koehler *et al* 1977).

In the proton radiotherapy facility of the National Cancer Center, Kashiwa, there are small-size normal conduction AVF cyclotron (C235) for medical purposes, two rotating gantry ports and one horizontal fixed port (Nishio 1999, Tachikawa *et al* 1999). To obtain laterally uniform irradiation fields, the dual-ring double scattering method is used in one rotating gantry port and the horizontal fixed port, and the wobbler method is used in the other rotating port.

To achieve uniform dose distribution in the irradiation field, the dual-ring double-scattering method requires much stricter initial conditions of incident beams entering the irradiation apparatus than the wobbler method (Takada 1994, 2002). If a rotating gantry is equipped, vertical sag due to the weight of the gantry affects the accuracy of the positions of each device. To achieve uniform dose distribution in the irradiation field and high reproducibility of the initial condition of beams, we developed a control system equipped with a mechanism for automatic fine adjustment of the beam incidence position and movement of the second dual-ring scatter to the optimal position.

2. Material and method

2.1. Apparatus for the formation of the irradiation field

The dual-ring double-scattering method consists of a profile monitor, a dual-ring double-scattering system, ring collimator (RC), ridge filter (RF), fine degrader (FD), dose monitor, flatness monitor, block collimator (BC), patient bolus (PB) and patient collimator (PC) (figure 1). Spread-out Bragg peak (SOBP) for the uniform dose distribution in the depth direction, which is produced by the aluminium wedge-shaped RF, can be selected from 8 grades between 30 mm and 100 mm in 10 mm steps for treatment. The FD is for the fine adjustment of the range to the target in the patient's body, the dose monitor is for the determination of the irradiation absolute dose, the flatness monitor is for the confirmation of the dose uniformity during irradiation of treatment beams, and the patient bolus and collimator are used for the shaping of beams based on the tumour size and form in each patient. Parameters for the formation of the individual irradiation field, SOBP, FD thickness, dose monitor value and patient bolus/collimator are determined for each patient and irradiation field.

The dual-ring double-scattering system of our centre is equipped with a uniform scatter made of Pb (first scatter) with variable thickness on the beam upstream side and another scatter with a dual-ring structure, the inner ring of which is made of Pb, and the outer one of Al (second scatter) on the beam downstream side. The thickness of the first scatter and the shape of the second scatter are determined by the energy of the proton beams. The second scatter can be moved three-dimensionally from 0 mm to 10 mm on the X- and Y-axis with the standard position, X, $Y = 5$ mm, and -100 mm to +100 mm on the Z-axis by remote control (see the dashed frame of figure 1). The maximum size of the irradiation field provided by the dual-ring double-scattering systems in the rotating gantry port is 200 mm ϕ.

The profile monitor consists of 8 air ionization dosimeters in the shape of a fan with 1/8 circle and is used for the observation of incidence proton beam axis and shape. The flatness

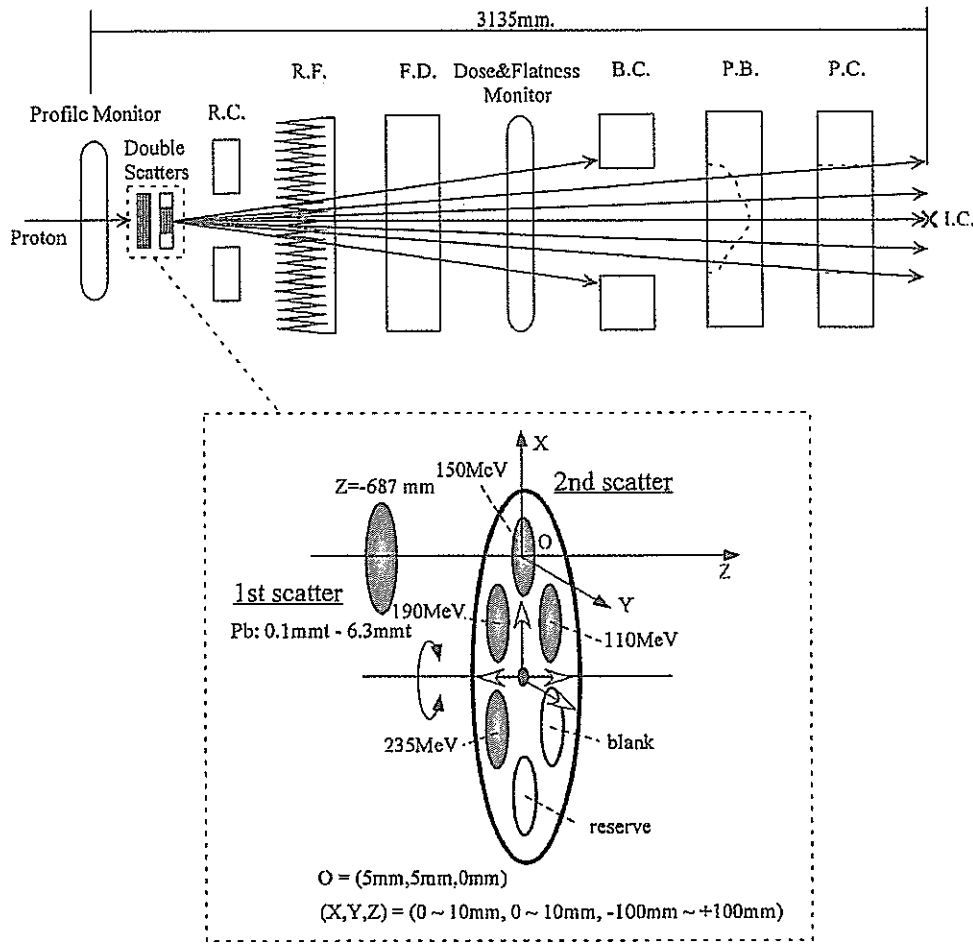

Figure 1. Arrangement of apparatus parts for the dual-ring double-scattering method.

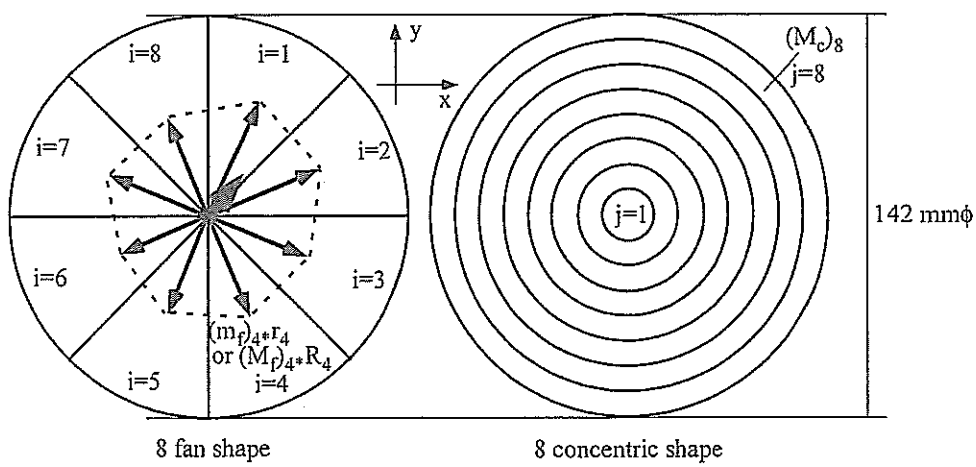

Figure 2. Illustration of the profile and flatness monitors.

monitor for the observation of uniformity of lateral dose distribution has a two-layer structure, with one layer consisting of 8 fan-shaped air ionization dosimeters (same shape as the profile monitor) and the other being 8 concentric air ionization dosimeters. The detailed shapes of the profile and flatness monitors are illustrated in figure 2. Profile monitor indication (PMI)

and flatness monitor indication (FMI) are defined as

$$\overrightarrow{\mathrm{PMI}}(I_f : x, y) = \sum_{i=1}^{8} (m_f)_i \cdot \vec{r}_i(x_i, y_i) = \begin{cases} \sum_{i=1}^{8} (m_f)_i \cdot x_i \\ \sum_{i=1}^{8} (m_f)_i \cdot y_i \end{cases}$$

$$= \begin{cases} \mathrm{PMI}(I_f : x) \\ \mathrm{PMI}(I_f : y) \end{cases}, \quad |\vec{r}_i| = 1 \text{ (8 fan shape)}, \tag{1}$$

$$\begin{cases} \overrightarrow{\mathrm{FMI}}(I_f : x, y) = \sum_{j=1}^{8} (M_f)_j \cdot \vec{R}_j(x_j, y_j) = \begin{cases} \sum_{j=1}^{8} (M_f)_j \cdot x_j \\ \sum_{j=1}^{8} (M_f)_j \cdot y_j \end{cases} \\ \qquad = \begin{cases} \mathrm{FMI}(I_f : x) \\ \mathrm{FMI}(I_f : y) \end{cases}, \qquad |\vec{R}_j| = 1 \text{ (8 fan shape)}, \\ \mathrm{FMI}(I_c) = \sum_{k=1}^{8} \left| \dfrac{(M_c)_k}{(M_c)_1 \cdot (2 \cdot k - 1)} - 1 \right| \qquad \text{(8 concentric shape)}. \end{cases} \tag{2}$$

Here, i, j and k denote identification of 8 fan and concentric separated areas, respectively. m_f, M_f and M_c are output signals from each separated area. In the profile monitor, the centre and symmetry are indicated by the length of the thick vector, $\mathrm{PMI}(I_f : x, y)$ and the shape formed with 8 thin vectors, $(m_f)_j \cdot r_j$, shown in figure 2. The beam approaches a centre position of the profile monitor as the length of the thick vector shortens. Similarly, in the flatness monitor, the symmetry and flatness of the dose profile are indicated by the length of the thick vector, $\mathrm{FMI}(I_f : x, y)$, and the value of $\mathrm{FMI}(I_c)$.

2.2. *Measurement of relationship between the incident beam conditions and uniformity of the dose distribution*

The dose distribution optimized in an irradiation field of 200 mm ϕ by the dual-ring double-scattering method is formed by the following equations (Takada 2002):

$$F(r) = f_{\mathrm{inner}}(r) + f_{\mathrm{outer}}(r),$$

$$f_{\mathrm{inner}}(r) = 1.80 \times 10^{-9} \cdot \exp(-8.90 \times 10^{-5} \cdot r^2) \int_0^{90} k \cdot \exp(-1.89 \times 10^{-4} \cdot k^2) \times \left[\int_0^{\pi} \exp(1.78 \times 10^{-4} \cdot r \cdot k \cdot \cos\theta)\, \mathrm{d}\theta \right] \mathrm{d}k, \tag{3}$$

$$f_{\mathrm{outer}}(r) = 1.06 \times 10^{-8} \cdot \exp(-5.22 \times 10^{-4} \cdot r^2) \int_{90}^{\infty} k \cdot \exp(-6.22 \times 10^{-4} \cdot k^2) \times \left[\int_0^{\pi} \exp(1.04 \times 10^{-3} \cdot r \cdot k \cdot \cos\theta)\, \mathrm{d}\theta \right] \mathrm{d}k.$$

Here, $f_{\mathrm{inner}}(r)$ and $f_{\mathrm{outer}}(r)$ denote the dose distribution components by the inner and outer rings of the second scatter, respectively, and r denotes the distance from the centre of the beam axis. Table 1 shows the conditions of the first and second scatters at each beam energy of 150 MeV, 190 MeV and 235 MeV. To obtain a dose distribution with a high degree of uniformity in the irradiation field, stability of the beam incidence position at the dual-ring scatter is very important.

The depth and lateral dose distribution for beam energies of 150, 190, 235 MeV, each SOBP, and FD in the field size of 200 mm are measured by changing the incident beam condition in the irradiation equipment. The measurement of the dose distribution is performed using a three-dimensional (3D) water phantom and an ionization chamber with a sensitive

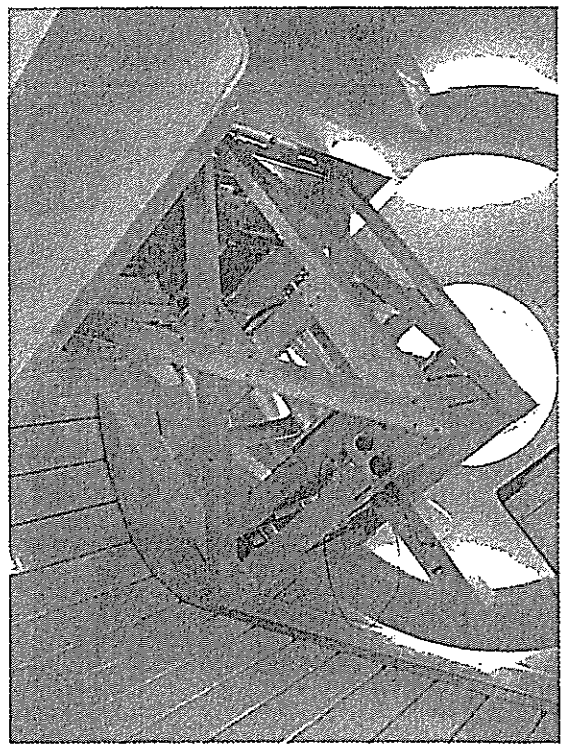

Figure 3. Picture of 3D water phantom.

Table 1. Thickness and characteristics of the first and second scatters.

Energy (MeV)	First scatter (Pb) thickness (mm)	Inside second scatter (Pb) thickness (mm)	Inside second scatter (Pb) diameter (mm)	Outside second scatter (Al) thickness (mm)
150	1.5	2.952	27.48	7.997
190	2.3	4.038	25.58	11.087
235	3.5	5.314	24.00	14.760

volume of 75 μl (figure 3). The 3D water phantom can rotate together with a nozzle of the rotating gantry. The depth and lateral dose distribution are measured by 1 mm and 2 mm step s^{-1}, respectively.

The uniformity of the measured lateral dose distribution was evaluated using parameters defined by the following symmetry and flatness (IEC 1989):

$$\text{Uniformity} = \begin{cases} \text{Symmetry} : S_{\text{FWHM}}\,[\%] = \dfrac{A_+ - A_-}{A_+ + A_-} \times 100, \\ \text{Flatness} : F_{0.8\times\text{FWHM}}\,[\%] = \dfrac{D_{\max} - D_{\min}}{D_{\max} + D_{\min}} \times 100. \end{cases} \tag{4}$$

The symmetry is expressed as the difference between the area on the '+' side of the lateral position (A_+) and the area on the '−' side of the lateral position (A_-) within an area of full-width at half-maximum (FWHM). The flatness is expressed as the difference between the maximal radiation dose ($D_{\max}$) and the minimal radiation dose ($D_{\min}$) within an area of 80% FWHM. The IEC (1989) report recommends symmetry of less than ±2% and flatness of less than 5%. However, the symmetry and flatness for proton radiotherapy are not regulated. In this study,

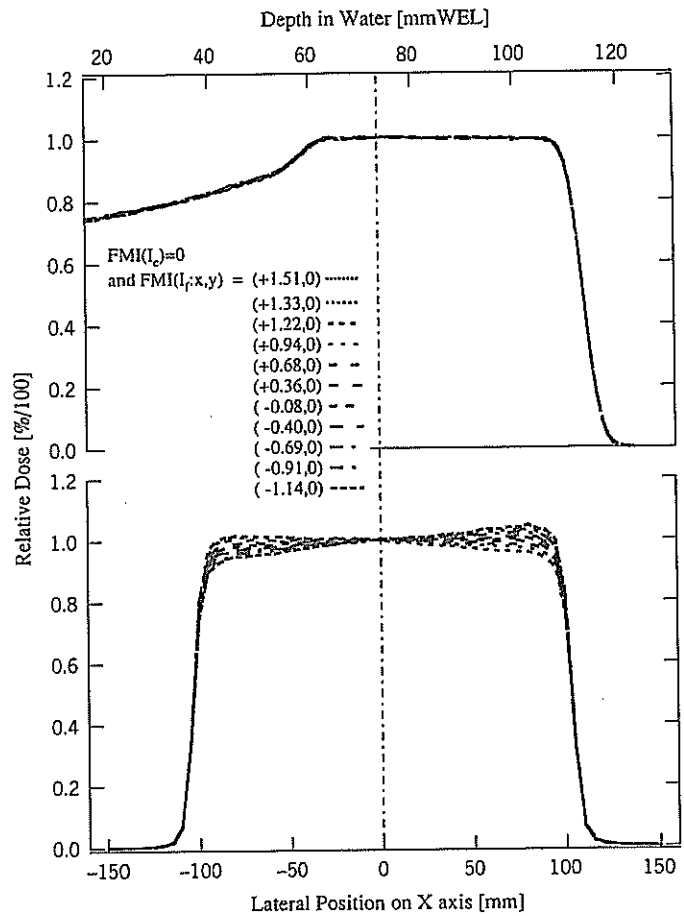

Figure 4. Depth and X-axis lateral dose distributions measured at $\overrightarrow{\mathrm{FMI}}(I_f : x, y) = (\mathrm{FMI}(I_f : x), 0)$ with $\mathrm{FMI}(I_c) \approx 0$ under the conditions of 150 MeV/SOBP 50 mm/Gantry = 0°.

we used symmetry of less than ±1% and flatness of less than 2.5% for the evaluation of proton radiotherapy.

3. Results and discussions

3.1. Correlation between the flatness monitor indication and uniformity of the dose distribution

The uniformity of the dose distribution in proton radiotherapy is observed using a flatness monitor. Figure 4 shows the depth and lateral dose distribution on the central axis of an SOBP measured at $\overrightarrow{\mathrm{FMI}}(I_f : x, y) = (-1.14, 0) \leftrightarrow (+1.51, 0)$ and $\mathrm{FMI}(I_c) \approx 0$ under the conditions of 150 MeV/SOBP 50 mm/Gantry = 0°. Figure 5 shows the symmetry and flatness of the lateral dose distribution measured at the flatness monitor indications under the conditions of 150 MeV/SOBP 50 mm/Gantry = 0°, 190 MeV/SOBP 80 mm/Gantry = 0° and 235 MeV/SOBP 80 mm/Gantry = 0°. These findings indicated that the uniformity of the dose distribution decreased by changing the $\overrightarrow{\mathrm{FMI}}(I_f : x, y)$ from the standard: $\overrightarrow{\mathrm{FMI}}(I_f : x, y) \approx (0, 0)$ and $\mathrm{FMI}(I_c) \approx 0$.

To satisfy a symmetry of less than ±1% and flatness of less than 2.5% in the dose distribution for proton radiotherapy, the $\mathrm{FMI}(I_f : x)$ and $\mathrm{FMI}(I_f : y)$ must be within ±0.03, respectively. Since no differences in the shape of the depth–dose distribution under different beam conditions were observed, it was not discussed in this study.

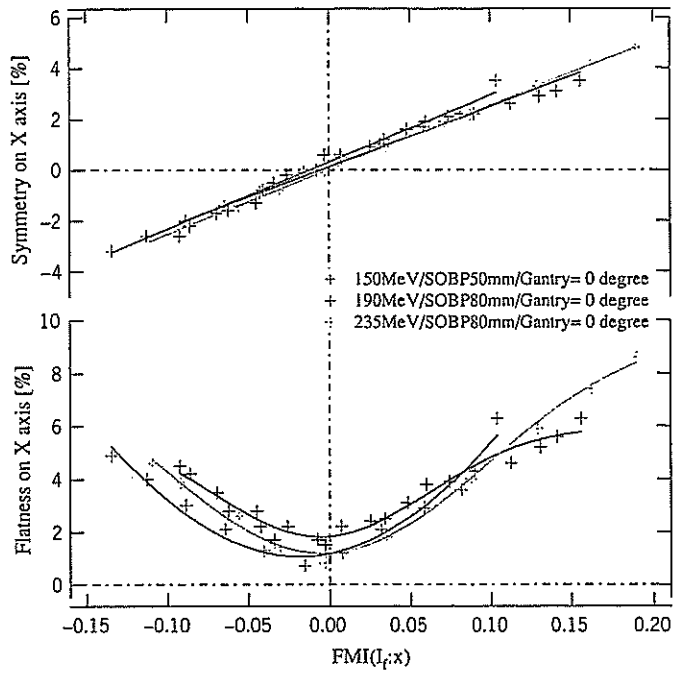

Figure 5. Symmetry and flatness of the X-axis lateral dose distribution measured at $\overrightarrow{\mathrm{FMI}}(I_f : x, y) = (\mathrm{FMI}(I_f : x), 0)$ with $\mathrm{FMI}(I_c) \approx 0$ under the conditions of 150 MeV/SOBP 50 mm/Gantry = 0°, 190 MeV/SOBP 80 mm/Gantry = 0°, and 235 MeV/SOBP 80 mm/Gantry = 0°.

3.2. Correlation between the profile monitor indication and the uniformity of the dose distribution with changes in the second scatter position

Figure 6 shows the uniformity of the dose distribution by mechanically moving the second scatter in 0.4 mm steps from the scatter position (−6 mm) with the initial beam condition for the uniform dose profile: $\overrightarrow{\mathrm{FMI}}(I_f : x, y) = (0, 0)$ and $\mathrm{FMI}(I_c) \approx 0$. Only the second scatter was moved in the constant beam condition ($\overrightarrow{\mathrm{FMI}}(I_f : x, y) \neq (0, 0)$). The movement value of the second scatter corresponded to the difference between the positions of the second scatter centre and the large Gaussian beam centre passing through the first scatter by the principle of the dual-ring double-scattering method. The uniformity of the dose distribution for proton radiotherapy is satisfied when the difference is less than 1 mm between the positions of the second scatter centre and the beam centre axis.

3.3. Correlation between the second scatter position and the profile monitor indication

The top graph of figure 7 shows the correlation between the incidence position of the beam observed by the profile monitor and the second scatter position. The second scatter was moved in a plane perpendicular to the beam axis so that the $\overrightarrow{\mathrm{FMI}}(I_f : x, y) = (0, 0)$ to the incidence beams. In the range of $|\overrightarrow{\mathrm{PMI}}(I_f : x, y)| \leqslant (1.0, 1.0)$, there was a linear correlation between the positions of the second scatter and incidence beams.

The middle and bottom graphs show the symmetry and flatness of the dose distribution with the second scatter position evaluated using equation (3). The results shown in figure 7 indicated that the flatness of the dose distribution required the $|\overrightarrow{\mathrm{PMI}}(I_f : x, y)| < (0.5, 0.5)$ and the second scatter position of 3–7 mm. The changes in the symmetry and flatness of the dose distribution caused by moving the second scatter were slower than those shown in figure 6. The beam centre always matches with the second scatter centre by movement

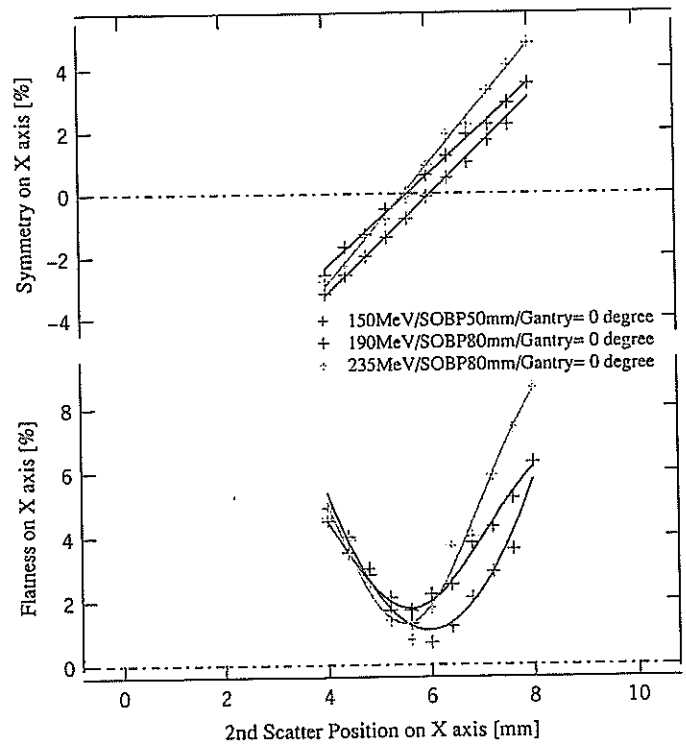

Figure 6. Symmetry and flatness of the X-axis lateral dose distribution by moving the second scatter under the conditions of 150 MeV/SOBP 50 mm/Gantry = 0°, 190 MeV/SOBP 80 mm/Gantry = 0°, and 235 MeV/SOBP 80 mm/Gantry = 0°.

of the second scatter position with $\overrightarrow{\mathrm{FMI}}(I_f : x, y) = (0, 0)$ in figure 7, but not with $\overrightarrow{\mathrm{FMI}}(I_f : x, y) \neq (0, 0)$ in figure 6. This indicated that the relationship of the relative position between the second scatter centre and beam axis centre was very important. In the stability of the beam from the proton accelerator, C235, since the irradiated beam conditions were not changed by $|\overrightarrow{\mathrm{FMI}}(I_f : x, y)| > (0.03, 0.03)$ during beam irradiation within about 10 min, the $\overrightarrow{\mathrm{FMI}}(I_f : x, y)$ always indicated a level close to zero during the proton treatment.

3.4. Control method for highly accurate uniformity of the dose distribution during proton treatment

To obtain uniformity of the dose distribution in the irradiation field by the dual-ring double-scattering method, the incident beam must satisfy strict conditions. If the central axis of beams moves more than 1 mm from the centre of the second scatter, the uniformity of the irradiation field becomes lower than the clinically useful level. The central axis of beams must be within the circle with a radius of 1 mm from the centre of the second scatter. In our institution, since changes in the beam axis during proton irradiation of less than 1 min for treatment are very small, there are no problems in maintaining uniformity of the dose distribution in the irradiation field if the central axis of beams is adjusted to agree with the centre of the second scatter before each irradiation. However, daily or long-term changes in the beams are larger than the accuracy required for the treatment, affecting the uniformity of the dose distribution.

To obtain highly accurate uniformity of the dose distribution in the irradiation field during proton radiotherapy, we developed a control system, consisting of functions for automatic fine adjustment of the central axis of beams and for placing the centre of the second scatter on the central axis of beams by moving the scatter mechanically. The central axis of beams is adjusted from the side closer to the beam source, brought about by a combination of the

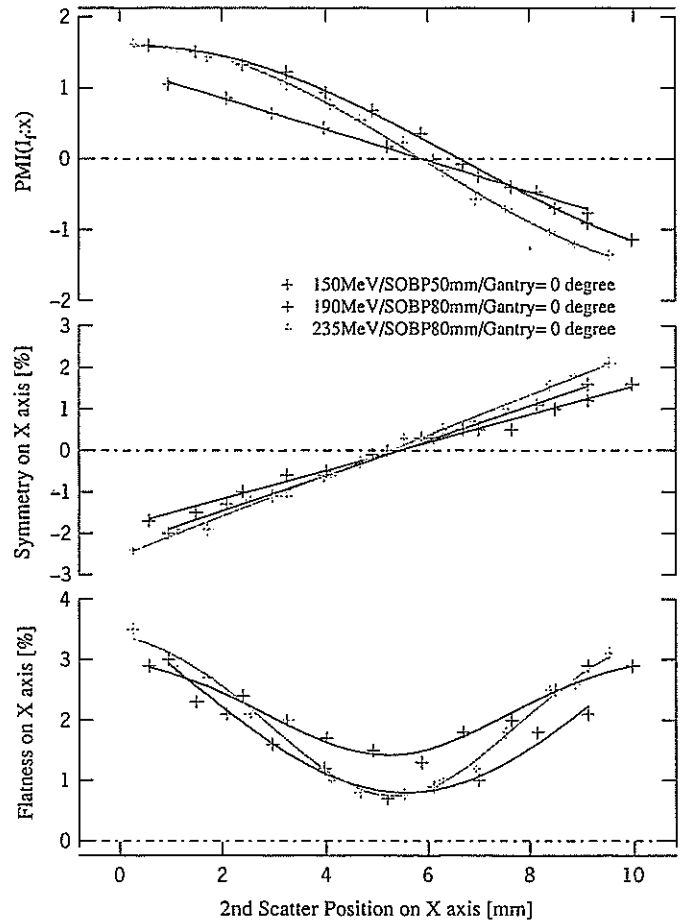

Figure 7. $\overrightarrow{\mathrm{PMI}}(I_f : x, y) = (\mathrm{PMI}(I_f : x), 0)$, symmetry, and flatness of the X-axis lateral dose distribution with respect to the position of the second scatter under the conditions of 150 MeV/SOBP 50 mm/Gantry = 0°, 190 MeV/SOBP 80 mm/Gantry = 0° and 235 MeV/SOBP 80 mm/Gantry = 0°.

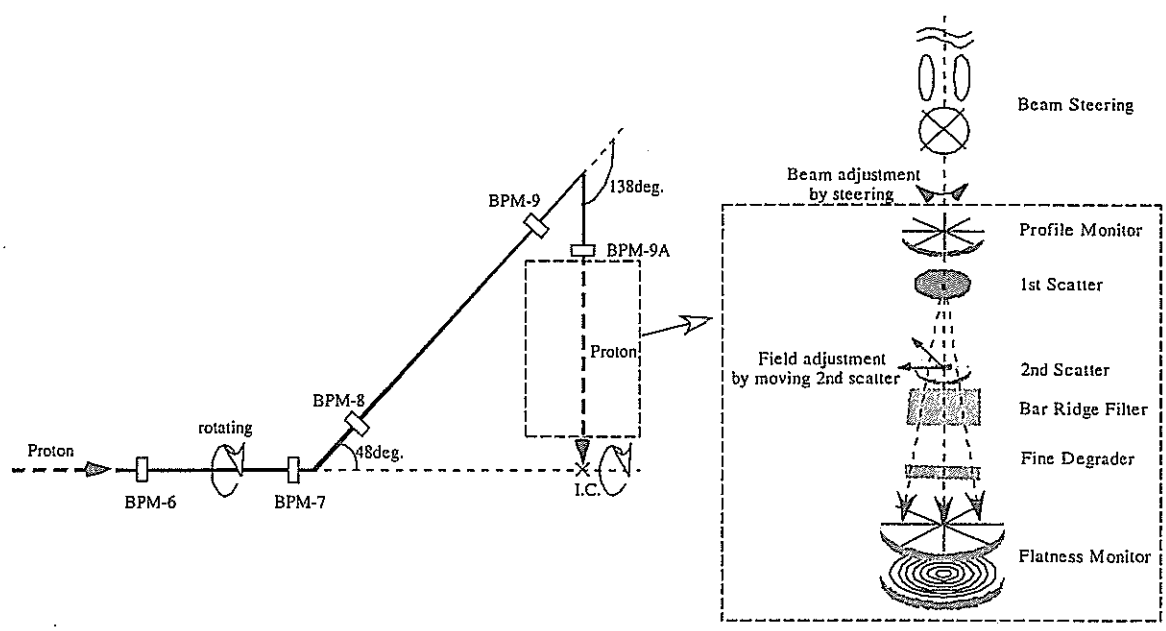

Figure 8. Arrangement of the beam profile monitor fixed in the rotating gantry and the outline of the irradiation apparatus for control of uniformity of the dose distribution at high accuracy.

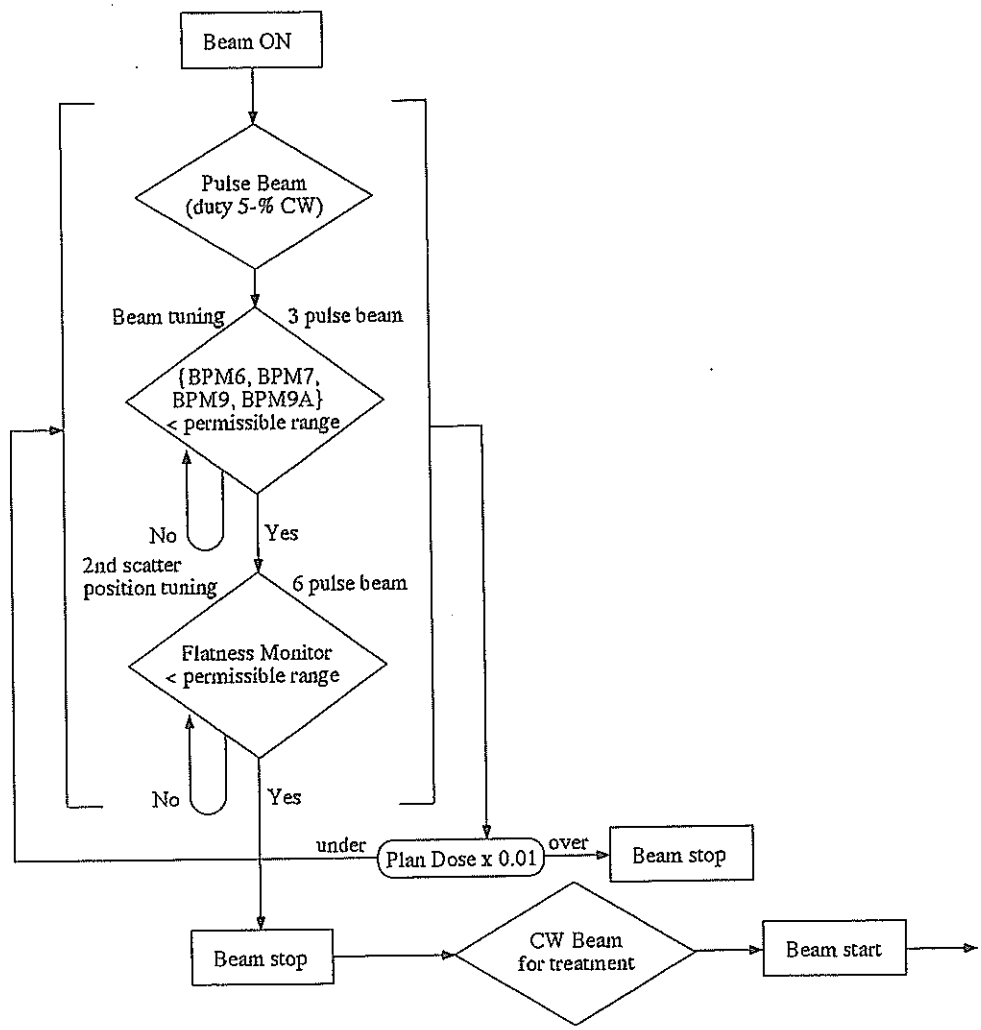

Figure 9. Flowchart of the control procedures for uniformity of the dose distribution at high accuracy.

beam profile monitor (BPM) fixed on the beam transport system of the rotating gantry and the steering electromagnet. The centre of the second scatter is adjusted to agree with the central axis of the incident beam by the profile and flatness monitors built into the irradiation apparatus (figure 8). After positioning the patient for treatment, the adjustment is performed by delivering pulsed proton beams to the patient with the settings for the treatment conditions prescribed for the patient, which is completed by an irradiation of less than 1% of the administration dose. Figure 9 shows the flowchart of the control procedures.

3.5. Results of the dose distribution uniformity by beams used in proton treatment

Figure 10 shows the characteristics of the correlation between the profile monitor indication and the centre of the second scatter under different conditions of proton irradiation after control of the dose distribution at high accuracy. In the figures obtained at the proton beam energies of 150 MeV, 190 MeV and 235 MeV, the symbols indicate all data for the condition of the SOBP width, the thickness of FD, the field size and the angle of the rotating gantry used in clinical treatment.

Taking the characteristics shown in figure 7 into consideration, the uniformity of the proton dose distribution in the irradiation field during treatment was at a level indicated by a symmetry of less than $\pm 1\%$ and flatness of less than 2%.

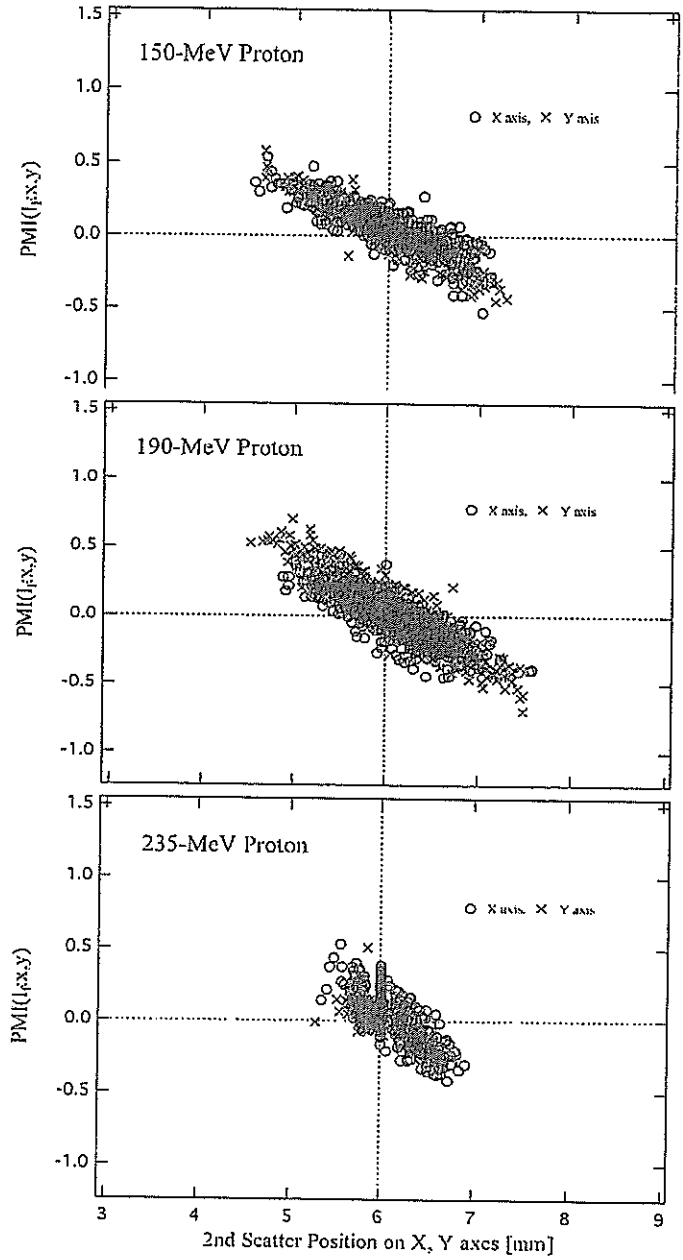

Figure 10. Characteristics of the correlation between the $\overrightarrow{\mathrm{PMI}}(I_f : x, y)$ and the centre of the second scatter after control of the dose distribution at high accuracy under different conditions of proton irradiation used in clinical treatment.

4. Conclusions

It is very difficult to obtain uniformity of the dose distribution in the irradiation field during proton radiotherapy by the dual-ring double-scattering method. Uniformity of the dose distribution during treatment could be obtained at high accuracy by using the control method that we developed. To adjust the central axis of beams to be within a circle with a radius of 1 mm, a high performance electromagnet and its power source would be required. Apparatus for proton radiotherapy with uniformity of the dose distribution at high accuracy can be provided to facilities to be built in the future at low costs using this control method.

Acknowledgments

We would like to thank the staff members of the Proton Radiotherapy Department of National Cancer Center Hospital East for help, the members of SHI Accelerator Service Ltd for the development of the apparatus, and the members of SHI Accelerator Service Ltd and Accelerator Engineering Inc. for the operation of the proton apparatus.

References

Chu W T, Ludewigt B A and Renner T R 1993 Instrumentation for treatment of cancer using proton and light-ion beams *Rev. Sci. Instrum.* **64** 2055–122

Graffman S, Jung B and Larsson B 1973 Design studies for a 200 MeV proton clinic for radiotherapy *6th Int. Cyclotron Conf. (Am. Inst. Phys., Vancouver, 1972)* vol 9 pp 603–15

IEC (International Electrotechnical Commission) 1989 *Medical Electrical Equipment*

Koehler A M, Schneider R J and Sisterson J M 1977 Flattening of proton dose distribution for large-field radiotherapy *Med. Phys.* **4** 297–301

Nishio T 1999 Present status and planning of facilities for proton and heavy ion cancer treatment in Japan—National Cancer Center *J. At. Energy Soc.* **41** 1134–8

PTCOG Newsletter 2004 PARTICLES 34 (July)

Tachikawa T, Sato T, Ogino T and Nishio T 1999 Proton treatment devices at National Cancer Center (Kashiwa, Japan) *Radiat. Indust.* **84** 48–53

Takada Y 1994 Dual-ring double scattering method for proton beam spreading *Japan. J. Appl. Phys.* **33** 353–9

Takada Y 2002 Optimum solution of dual-ring double scattering system for an incident beam with given phase space for proton beam spreading *Nucl. Instrum. Methods* A **485** 255–76

Available online at www.sciencedirect.com
SCIENCE DIRECT
ELSEVIER
Immunology Letters 101 (2005) 160–167
Immunology Letters
www.elsevier.com/locate/

Cytokine production and migration of in vitro-expanded NK1.1$^-$ invariant Vα14 natural killer T (Vα14i NKT) cells using α-galactosylceramide and IL-2

Yoshinori Ikarashi[a,*], Akira Iizuka[a,b,c], Yuji Heike[a], Mitsuzi Yoshida[a], Yoichi Takaue[b], Hiro Wakasugi[a,*]

[a] *Pharmacology Division, National Cancer Center Research Institute, 5-1-1, Tsukiji, Chuo-ku, Tokyo 104-0045, Japan*
[b] *Hematopoietic Stem Cell Transplantation/Immunotherapy Unit, National Cancer Center Hospital, Tokyo, Japan*
[c] *Department of Pathology and Immunology, Aging and Developmental Sciences, Graduate School, Tokyo Medical and Dental University, Tokyo 113-8519, Japan*

Received 31 March 2005; received in revised form 25 May 2005; accepted 26 May 2005
Available online 20 June 2005

Abstract

Mouse natural killer T cells with invariant Vα14 rearrangement (Vα14i NKT cells) can rapidly produce both Th1 and Th2 cytokines and regulate various immune responses, such as autoimmunity and tumor immunity. In this study, we describe the phenotypical and functional characterization of in vitro-expanded mouse Vα14i NKT cells from spleen using a combination of α-galactosylceramide (α-GalCer) and IL-2. The expanded Vα14i NKT cells retained the memory/activated (CD44$^+$CD69$^+$CD62L$^-$) and CD4$^+$ or CD4$^-$8$^-$ double negative phenotypes but modulated or lost the classical NKT cell marker, NK1.1. The expanded Vα14i NKT cells continuously released IL-4 and IFNγ and induced NK cell IFNγ production in vitro. Furthermore, the expanded Vα14i NKT cells migrated into the liver and spleen after adoptive transfer into lymphopenic SCID mice, and they were able to rapidly produce IL-4 and IFNγ after α-GalCer injection. Our findings suggest that the intrinsic characteristics of the cytokine secretion of Vα14i NKT cells were equivalent to that of in vitro-expanded Vα14i NKT cells. In vitro-expanded Vα14i NKT cells are considered to be useful for NKT cell defect-related diseases, such as autoimmunity and cancer.

Keywords: CD1d; α-Galactosylceramide; NKT cell; Cytokine

1. Introduction

Mouse natural killer T cells with an invariant Vα14-Jα18 TCR rearrangement (Vα14i NKT cells) preferentially associate with Vβ8.2, Vβ7 or Vβ2 TCR, recognize glycolipid antigens in the context of the non-classical MHC class I molecule CD1d [1–3], and respond strongly to a synthetic glycolipid, α-galactosylceramide (α-GalCer) [1–3]. The Vα14i NKT cells display a memory or activated phenotype (CD44^{high}CD62L$^-$CD69$^+$) and express NK cell markers, such as NK1.1 [1–3]. A feature of Vα14i NKT cells is the rapid secretion of several immunoregulatory cytokines, such as Th1 cytokines (IFNγ) and Th2 cytokines (IL-4 and IL-10) [1–3]. Cytokine production by Vα14i NKT cells plays an important role in various immune responses, including autoimmunity and tumor-immunity.

Vα14i NKT cells have antitumor activities [4,5]. Vα14i NKT cells exhibit direct cytotoxicity against various tumor cell lines [6] and rapidly produce IFNγ to induce NK cell activation [7,8]. Furthermore, the administration of α-GalCer, a specific ligand for Vα14i NKT cells, prevents tumor metastasis [9,10], and the antimetastatic activity of α-GalCer is mediated by sequential production of IFNγ by Vα14i NKT cells and NK cells [11,12].

* Corresponding authors. Tel.: +81 3 3547 5248; fax: +81 3 3542 1886.
E-mail addresses: yikarash@gan2.ncc.go.jp (Y. Ikarashi), hwakasug@gan2.ncc.go.jp (H. Wakasugi).

0165-2478/$ – see front matter © 2005 Elsevier B.V. All rights reserved.
doi:10.1016/j.imlet.2005.05.007

In humans, NKT cells with invariant Vα24 chains paired with Vβ11 chains (Vα24i NKT cells) are the counterpart to mouse Vα14i NKT cells, and they also respond to α-GalCer and rapidly secrete IFNγ and IL-4 [1–3]. Several investigators have reported the robust expansion of human Vα24i NKT cells from peripheral blood mononuclear cells (PBMCs) using α-GalCer plus a combination of cytokines, such as IL-2, IL-7 and IL-15, in vitro [13–18]. α-GalCer-loaded dendritic cells and IL-2 also can induce the expansion of $V\alpha24^+$ NKT cells from PBMCs [15,18]. After culture with α-GalCer and cytokines, the expanded human Vα24i NKT cells retain the ability to produce IFNγ and IL-4 [15,19], and they exhibit cytotoxic activity against tumor cell lines [20,21]. Recent studies have revealed significant reductions in numbers of Vα24i NKT cells and deficiencies in their proliferative responses and IFNγ production of Vα24i NKT cells in some patients with advanced cancer [22,23]. Therefore, adoptive transfer of in vitro-expanded Vα24i NKT cells is expected to induce antitumor activities in cancer patients with reduced circulating Vα24i NKT cell numbers.

It has been reported that mouseVα14i NKT cells also respond to α-GalCer by proliferating in vitro [1–3]. However, little is known regarding the function and phenotype of in vitro-expanded Vα14i NKT cells because hitherto there was no appropriate marker to identify these cells. In this study, we used CD1d/α-GalCer tetramer to monitor Vα14i NKT cells. We demonstrate that splenic Vα14i NKT cells can be expanded up to 8-fold after 4 days of culture with α-GalCer and IL-2. In vitro-expanded Vα14i NKT cells migrate to the liver and spleen of recipient mice and produce IFNγ and IL-4 in vivo after administration of α-GalCer.

2. Material and methods

2.1. Mice

Female C57BL/6N mice, BALB/cAnN mice and C.B-17/Icr SCID mice were purchased from Charles River Japan Inc. (Kanagawa, Japan). All mice were used at 8–12 weeks of age and maintained in our facilities. Animal studies were performed according to guidelines from the animal experimental ethics committee.

2.2. Cell culture

Spleen, liver, thymus and bone marrow mononuclear cells were prepared as previously described [24]. Mononuclear cells (1×10^6 cells/ml) were cultured in 7 ml of RPMI 1640 medium (Invitrogen Corp., Carlsbad, CA) supplemented with 8% fetal calf serum (JRH Biosciences, Lenexa, KS), 5×10^{-5} M 2-mercaptoethanol (Sigma–Aldrich, Saint Louis, MO), 2 mM L-glutamine (Invitrogen), 1 mM sodium pyruvate (Invitrogen), 0.1 mM non-essential amino acids (Invitrogen), 100 U/ml penicillin and 100 μg/ml streptomycin (Invitrogen) in 25 cm^2 culture flask (Greiner Bio-One GmbH, Germany). α-GalCer (50 ng/ml; Pharmaceutical Research Laboratory, Kirin Brewery, Gunma, Japan) and/or recombinant human IL-2 (100 IU/ml; Takeda Chemical Ind. Ltd., Osaka, Japan) were added to the culture. On day 4, non- and semi-adherent cells were harvested, spun down and resuspended in the medium. The cells (5×10^5 cells/ml) were cultured in 7 ml of the medium in the presence of α-GalCer and/or IL-2 for an additional 2 days.

2.3. Flow cytometry

The surface phenotype of cells was determined by multicolor flow cytometry as previously described [24]. Before staining cells with mAb, cells were pre-incubated with anti-CD16/32 (clone 2.4G2) to block non-specific FcRγ binding. The following antibodies were used in this study: FITC- or PE-conjugated anti-CD3 (clone 145-2C11) or anti-CD24 (clone M1/69), PE-conjugated anti-NK1.1 (clone PK136), anti-CD69 (clone H1.2F3), or anti-IL-2Rβ (clone TM-β1), and APC-conjugated mouse CD1d tetramers loaded with α-GalCer (CD1d/α-GalCer tetramers). Stained cells were analyzed using a FACSCalibur equipped with CELLQuest software (BD Biosciences, San Jose, CA). Dead cells were excluded by propidium iodide staining and electronic gating. The data were processed with Flow Jo software (Tree Star, San Carlos, CA). For intracellular staining, cells were stimulated for 2 h with 25 ng/ml PMA and 1 μg/ml ionomycin. The cells were then washed and incubated with anti-CD16/32, stained with PE-conjugated α-GalCer/CD1d tetramers, permeabilized with Cytofix/Cytoperm (BD PharMingen), and stained with APC-conjugated anti-IL-4 (clone 11B11), IFNγ (clone XMG1.2), or rat IgG1 isotype control (clone R3-34). The stained cells were analyzed using a FACSCalibur. All mAbs were purchased from BD PharMingen. PE- or APC-conjugated CD1d/α-GalCer tetramers were prepared in a baculovirus expression system as previously described [25]. Mouse CD1d/β2-microglobulin expression vector was provided by Dr. M. Kronenberg (La Jolla Institute for Allergy and Immunology, San Diego, CA).

2.4. Cytokine levels

Culture supernatants were collected following 1, 4, or 6 days of culture and stored at −20 °C before analysis. IFNγ and IL-4 concentrations in culture supernatants were determined by ELISA kits (OptEIA ELISA set; BD PharMingen).

2.5. Adoptive transfer of in vitro-expanded Vα14i NKT cells

Spleen cells from BALB/cAnN mice were culture in the presence of α-GalCer and IL-2 for 4 days. The cultured spleen cells containing expanded Vα14i NKT cells (2×10^7) were transferred i.v. to C.B-17/Icr SCID mice. The recipient mice were killed on day 7 after cell transfer, and the percentage of CD1d/α-GalCer $tetramer^+$ cells in the spleen and liver were

determined by flow cytometry. The serum levels of IFNγ and IL-4 in mice injected with cultured cells 7 days earlier were analyzed at 0, 4, and 10 h after i.p. injection of α-GalCer (2 μg).

3. Results

3.1. Expansion of mouse Vα14i NKT cells in vitro

Consistent with previous results [25,26], we observed that 1.2% of freshly isolated spleen cells comprised Vα14i NKT cells (Fig. 1A). When spleen cells were cultured in the presence of 50 ng/ml α-GalCer, the percentage and absolute number of Vα14i NKT cells increased to 6.7% and 8-fold, respectively, after 4 days culture (Fig. 1). α-GalCer-induced human $Vα24^+Vβ11^+$ NKT cell expansion can be potentiated by IL-2, IL-7, or IL-15 [13–18]. To examine whether IL-2 augments mouse Vα14i NKT cell expansion by α-GalCer, spleen cells were cultured in the presence of α-GalCer and 100 U/ml IL-2. Vα14i NKT cells were more vigorously expanded when cultured with α-GalCer and IL-2 as compared with α-GalCer alone. IL-15 also enhanced α-GalCer-induced Vα14i NKT cell expansion (data not shown). Vα14i NKT cell expansion peaked after 4 days of culture with α-GalCer alone, whereas IL-2 prolonged Vα14i NKT cell expansion by α-GalCer past 4 days in culture (Fig. 1B). Furthermore, Vα14i NKT cells in thymus, liver, and bone marrow could be expanded in the presence of α-GalCer and IL-2 (data not shown). However, Vα14i NKT cells were not expanded in the presence of IL-2 alone (Fig. 1). It should be noted that in vitro expansion of Vα14i NKT cells is dependent on α-GalCer.

$NK1.1^+$ T cells, which are classical NKT cells, increased to around 5-fold after 4 days culture in the presence of IL-2 with or without α-GalCer (Fig. 1). Furthermore, they increased to around 20-fold after 6 days culture. Like $NK1.1^+$ T cells, NK cells expanded in the presence of IL-2. Thus, the expansion of $NK1.1^+$ T cells and NK cells is dependent on IL-2 but not α-GalCer.

3.2. Phenotypes of in vitro-expanded Vα14i NKT cells

Because the expansion of Vα14i NKT cells and $NK1.1^+$ T cells was dependent on α-GalCer and IL-2, respectively, we next examined whether the Vα14i NKT cells were identical to $NK1.1^+$ NKT cells after culture with α-GalCer and IL-2. Consistent with previous studies [25,26], half of $NK1.1^+$ T cells were CD1d/α-GalCer $tetramer^+$ cells and around 70% of Vα14i NKT cells expressed NK1.1 in the spleen (Fig. 2A). However, after culture, almost all Vα14i NKT cells lost expression of NK1.1. Our results indicate that the expanded Vα14i NKT cells are distinct from the expanded $NK1.1^+$ T cells following in vitro culture.

We analyzed the phenotype of the expanded Vα14i NKT cells as compared with fresh Vα14i NKT cells. As shown in Fig. 2B, the expanded Vα14i NKT cells maintained memory

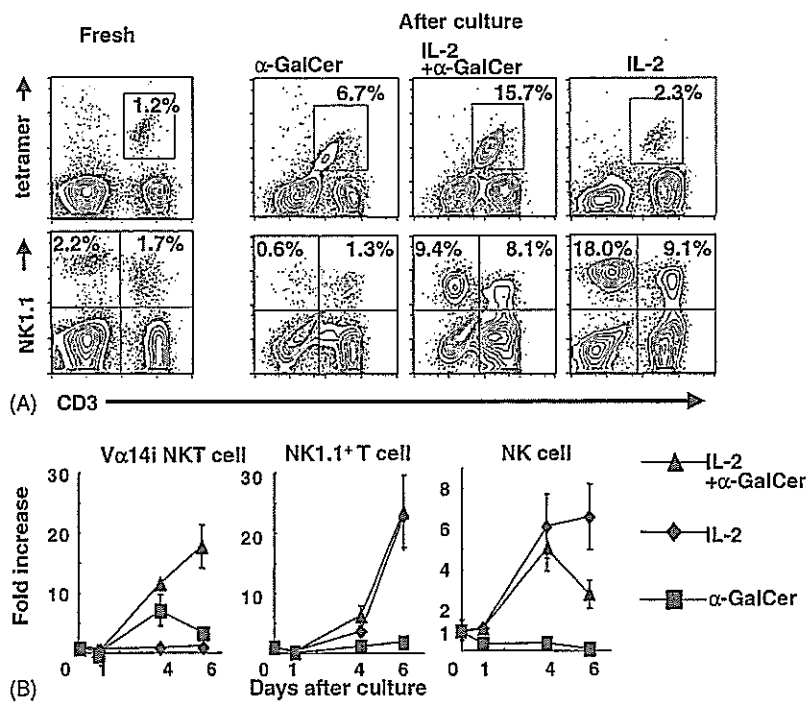

Fig. 1. In vitro expansion of Vα14i NKT cells. (A) C57BL/6 mice spleen cells (7×10^6) were cultured with 50 ng/ml α-GalCer, α-GalCer plus 100 U/ml IL-2, or IL-2 for 4 days. The percentages of Vα14i NKT cells, NK cells, and $NK1.1^+$ T cells were determined. Fresh and cultured cells were stained with mAbs and CD1d/α-GalCer tetramer and analyzed by flow cytometry. The fluorescence profiles are representative of at least five independent experiments. (B) The fold increase in Vα14i NKT cells after culture with IL-2 plus α-GalCer (▲), IL-2 alone (◆), or α-GalCer alone (■) was calculated from cell counts and flow cytometric data. Data are means obtained from three mice per point.

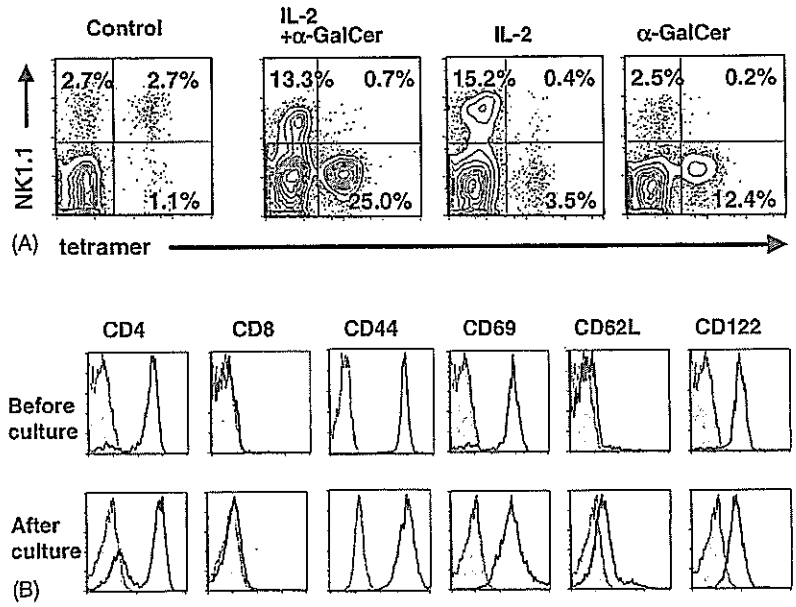

Fig. 2. Phenotype of in vitro-expanded Vα14i NKT cells. (A) NK1.1 expression in in vitro-expanded Vα14i NKT cells was examined after 4 days culture. Fresh and cultured cells were stained with CD1d/α-GalCer tetramer, anti-CD3, and anti-NK1.1 mAb. The cells were analyzed by flow cytometry and gated on CD3-positive cells. The fluorescence profiles are representative of at least five independent experiments. (B) The surface marker expression of fresh and expanded Vα14i NKT cells was compared by flow cytometry. Histogram panels are gated on CD1d/α-GalCer tetramer$^+$ CD3$^+$ cells. Shadow histograms indicate non-stained controls. The fluorescence profiles are representative of at least three independent experiments.

or activated phenotypes (CD44^{high}CD62L$^-$CD69$^+$) whereas the expression of IL-2Rβ was down-regulated. Similar to fresh Vα14i NKT cells, the expanded Vα14i NKT cells consisted of CD4$^+$ and CD4$^-$CD8$^-$ double negative subsets (Fig. 2B). In addition, some expanded Vα14i NKT cells maintained CD94 expression and down-regulated NKG2D, although some fresh Vα14i NKT cells express NK receptors, such as CD94 and NKG2D (data not shown). These results indicate that expanded Vα14i NKT cells maintain the memory or activated phenotypes but modulate the expression of NK cell-related molecules.

3.3. *In vitro-expanded Vα14i NKT cells retain the ability to produce cytokines*

It has been reported that α-GalCer induces rapid activation of Vα14i NKT cells and a burst of IL-4 and IFNγ secretion in vivo and in vitro [8–10]. Therefore, we examined the ability of expanded Vα14i NKT cells to secrete IL-4 and IFNγ. First, we analyzed IL-4 and IFNγ levels in the supernatants of spleen cells cultured with α-GalCer and/or IL-2 (Fig. 3A). We detected a larger amount of IL-4 and IFNγ in the supernatant when cultured in the presence of α-GalCer. Furthermore, the addition of IL-2 to the culture with α-GalCer slightly enhanced the production of IL-4 and IFNγ. No IL-4 and a low amount of IFNγ were detected when spleen cells were cultured with IL-2 alone.

Next, we used intracellular cytokine staining to determine if expanded Vα14i NKT cells directly secrete IL-4 and IFNγ in vitro (Fig. 3B). IL-4 producing cells comprised mainly expanded Vα14i NKT cells. Seventy percent of expanded Vα14i NKT cells contained intracellular IFNγ. These results suggest that expanded Vα14i NKT cells retain the ability to produce cytokines in vitro. In addition to expanded Vα14i NKT cells, 70% of CD1d/α-GalCer tetramer$^-$ T cells and 40% of CD1d/α-GalCer tetramer$^-$ CD3$^-$ cells were also positive for intracellular IFNγ. The IFNγ producing CD1d/α-GalCer tetramer$^-$ CD3$^-$ cells were mainly NK cells but not B cells (data not shown). It should be noted that NK cells and some T cells acquired the ability to produce IFNγ when cultured with α-GalCer and IL-2 but not IL-2 alone.

3.4. *In vivo survival and cytokine production of expanded Vα14i NKT cells after adoptive transfer*

We examined the ability of expanded Vα14i NKT cells to survive and migrate to peripheral tissues after adoptive transfer. Spleen cells cultured with α-GalCer and IL-2 were transferred into lymphopenic SCID mice. Seven days after transfer, the mice were killed and the CD1d/α-GalCer tetramer$^+$ cells in the liver and spleen were analyzed. As shown in Fig. 4, around 7% of hepatic mononuclear cells were CD1d/α-GalCer tetramer$^+$ T cells. The percentage of CD1d/α-GalCer tetramer$^+$ cells in the spleen was equal to that observed in normal mice (Figs. 1A and 4). Although it has been known that Vα14i NKT cells are abundant in bone marrow in normal mice, we observed very few CD1d/α-GalCer tetramer$^+$ cells in bone marrow (data not shown). The expanded Vα14i NKT cells were detected at least 3 weeks after transfer (data not shown). There were no differences in the phenotype of in vitro-expanded Vα14i NKT cells before and after transfer into SCID mice.